

Impacts of Hurricane Irma (2017) on ocean transport processes

Thomas Dobbelaere^{a,*}, Milan Curcic^b, Matthieu le Hénaff^{c,d}, Emmanuel Hanert^{a,e}

^a*Eath and Life Institute (ELI), UCLouvain, Louvain-la-Neuve, Belgium*

^b*Rosenstiel School of Marine and Atmospheric Sciences (RSMAS), University of Miami, Coral Gables, Florida, USA*

^c*Cooperative Institute for Marine and Atmospheric Studies (CIMAS), University of Miami, Miami, Florida, USA*

^d*Atlantic Oceanographic and Meteorological Laboratory (AOML), NOAA, Miami, Florida, USA*

^e*Institute of Mechanics, Materials and Civil Engineering (IMMC), UCLouvain, Louvain-la-Neuve, Belgium*

Abstract

Tropical cyclones are becoming more intense and more frequent. Their effect is particularly acute in coastal areas where they cause extensive damage leading to an influx of debris, sediments and waste to the sea. However, most coastal ocean models do not represent their transport correctly as they do not couple the hydrodynamics with the wind-generated waves. This may lead to significant errors in heavy-wind conditions. Here, we investigate current-wave interactions during a major cyclone and assess their impact on transport processes. We do that by coupling the unstructured-mesh coastal ocean model SLIM with the spectral wave model SWAN, and applying it to the Florida Reef Tract during Hurricane Irma (Sept. 17). We show that the coupled model successfully reproduces the wave behaviour, the storm surge and the ocean currents during the passage of the hurricane. We then use the coupled and uncoupled wave-current model to simulate the transport of

*Corresponding author

Email address: thomas.dobbelaere@uclouvain.be (Thomas Dobbelaere)

passive drifters. We show that the wave force alone can lead to changes of up to 1 m/s in the modelled currents, which in turn lead to differences of up to 10 km in the position of drifting material over the duration of the hurricane. [Add a sentence on Stokes drift vs wave-current coupling]. Our results suggest that wave-current interactions can strongly impact the transport of drifting material such as sediments and debris in the aftermath of a hurricane. They should thus be taken into account in order to correctly assess its overall impact

Keywords:

1. Introduction

Tropical cyclones are becoming more intense and more frequent (Bhatia et al., 2019; Kossin et al., 2020). This increase is likely due to climate change and will probably continue in the future (Knutson et al., 2020). However, estimating the impact of tropical cyclones on the coastal ocean circulation remains a challenge. Understanding wave-current interactions and being able to represent their impact on coastal ocean transport processes is central to many coastal activities such as dredging, erosion management, O&G, search and rescue (Bever and MacWilliams, 2013; Li and Johns, 1998; Breivik et al., 2013). It would for instance allow to predict hurricane impacts in events such as the Deepwater Horizon oil spill in the Gulf of Mexico in 2010 (Le Hénaff et al., 2012).

Wave-current interactions during a cyclone are highly nonlinear and can vary significantly in space and time (Wu et al., 2011). Wave-induced currents are generated by wave radiation stress gradients (Longuet-Higgins, 1970), affecting water levels near shorelines and wave breaking points (Longuet-Higgins and Stewart, 1964). Changes in water levels and currents, in turn, affect the motion and evolution of the waves (Sikirić et al., 2013). Coupled wave-current models are therefore required to capture these complex interactions. In order to accurately include surface waves in their equations, such models require the

21 computation of the the full two-dimensional wave spectrum (Van Den Bremer
22 and Breivik, 2018). Spectral wave model are therefore needed.

23 Coastal oceans are characterized by the complex topography of the coast-
24 line and the presence of islands, reefs and artificial structures. Traditional
25 structured-grid models often lack the flexibility to simulate near-shore pro-
26 cesses at a sufficiently small scale. Instead, unstructured-mesh models can
27 easily adapt to the topography and are hence better suited to coastal processes
28 (Wu et al., 2011; Chen et al., 2007). Being able to capture the impact of the
29 topography on wave interactions becomes even more important in the case of
30 tropical cyclones. Heavy winds generate large wind-waves and disturb ocean
31 conditions (Liu et al., 2020) by causing coastal upwellings on continental
32 shelves (Smith, 1982) and inducing strong currents, waves and storm surges
33 in nearshore and coastal regions (Dietrich et al., 2010; Weisberg and Zheng,
34 2006).

35 The transport of drifting objects or substances that are locally released
36 is often best represented by a Lagrangian individual-based model. Such
37 an approach is routinely used to model the dispersal of larvae, pollutants,
38 sediments and many other tracers (e.g. Le Hénaff et al. (2012); Liubartseva
39 et al. (2018); Figueiredo et al. (2013); Frys et al. (2020)). Although some
40 transport models take the impact of waves into account by adding a Stokes
41 drift velocity, *i.e.* the net drift of a floating particle in the direction of the wave
42 propagation (Van Den Bremer and Breivik, 2018), to the Eulerian currents,
43 they usually neglect the wave-induced currents. Such practice is reasonable
44 in the case of fair weather, when wave-induced forces exerted on currents are
45 relatively small, but might lead to significant errors during storm conditions
46 (Röhrs et al., 2012; Curcic et al., 2016).

47 The objective of this study is therefore to assess the importance of wave-
48 current interactions during a tropical cyclone. We investigate the transport
49 of drifting particles on the Florida shelf during Hurricane Irma, one of the
50 strongest and costliest tropical cyclones on record in the Atlantic Basin (Xian

et al., 2018), which made landfall in Florida in September 2017. To do that, we developed an unstructured coupled wave-current model of South Florida to simulate the ocean circulation during hurricane Irma. Both modelled currents and waves were validated against field measurements and were then used to simulate the transport of drifting material in the Florida Keys and the Florida inner shelf. Model outputs were then compared with uncoupled simulation results in order to assess the impact of wave-induced forces and Stokes drift on the modelled currents and transports.

2. Methods

2.1. Study area and observational data

The large-scale ocean circulation around South Florida is dominated by the Florida Current (FC), which originates from the Loop Current (LC) where it enters the Florida Straits from the Gulf of Mexico, and, downstream, forms the Gulf Stream. The FC is a major western boundary current characterized by spatial variability and meandering, associated with the presence of cyclonic eddies between the core of the current and the complex reef topography of the Florida Reef Tract (FRT) (Lee et al., 1995; Kourafalou and Kang, 2012). The variability of the FC extends over a large range of spatial and temporal scales, with periods of 30-70 days in the Lower Keys (Lee et al., 1995) and shorter periods of 2-21 days in the Upper Keys (Lee and Mayer, 1977), and exhibits significant seasonal and interannual cycles (Johns and Schott, 1987; Lee and Williams, 1988; Schott et al., 1988). Circulation on the West Florida Shelf (WFS) on the other hand is forced by local winds and tidal fluctuations (Lee and Smith, 2002; Liu and Weisberg, 2012). Furthermore, due to its location relative to the warm waters of the North Atlantic, Florida is particularly vulnerable to tropical cyclones. On average, the state gets hit by a hurricane every two years and strong hurricanes, some of which the most destructive on record, strike Florida on average once every four years. Malmstadt et al. (2009).

80 The state of the ocean around Florida is monitored by an extensive
81 array of tide gauges, current meters and buoys. In this study, we used sea
82 surface elevation measurements from the National Oceanic and Atmospheric
83 Administrations (NOAA) Tides and Currents dataset. These measurements
84 were taken at four locations: two in the Florida Keys (Key West and Vaca Key);
85 one on the eastern coast of Florida (Virginia Key); and one on the western
86 coast (Naples). For the currents, we used ADCP measurements from the
87 University of South Florida's College of Marine Science's (USF/CMS) Coastal
88 Ocean Monitoring and Prediction System (COMPS) for the WFS (Weisberg
89 et al., 2009). More specifically, we used measurements from moorings C10,
90 C12 and C13, respectively located at the 25, 50, and 50 m isobaths of the
91 WFS (Liu et al., 2020). Finally, for the waves, we used measurements from
92 four buoys of the NOAA's National Data Buoy Center (NDBC); two on
93 Florida's eastern shelf and two on the WFS. The locations of all measurement
94 stations are shown in Fig. 1A,C.

95 *2.2. Wind and atmospheric pressure during Hurricane Irma*

96 Irma made landfall in Florida on 10 September 2017 as a category 3
97 hurricane, first at Cudjoe Key (Florida Keys) and later on Marco Island,
98 south to Naples (see hurricane track in Fig. 1). It then weakened to a
99 category 2 hurricane as it moved further inland (Pinelli et al., 2018). The
100 storm damaged up to 75% of the buildings at its landfall point in the Florida
101 Keys, making it one of the strongest and costliest hurricanes on record in the
102 Atlantic basin (Xian et al., 2018; Zhang et al., 2019). The strongest reported
103 wind speed was 50 m/s on Marco Island while the highest recorded storm
104 surge was 2.3 m, although larger wind speed likely occurred in the Florida
105 Keys (Pinelli et al., 2018). In order to reproduce the wind profile of Irma in
106 our model, we used high-resolution H*Wind wind fields (Powell et al., 1998).
107 As these data represent 1-min averaged wind speeds, we multiplied them by a
108 factor 0.93 to obtain 10-min averaged wind speeds (Harper et al., 2010), which
109 are more consistent with the time step of our model. Furthermore, H*Wind

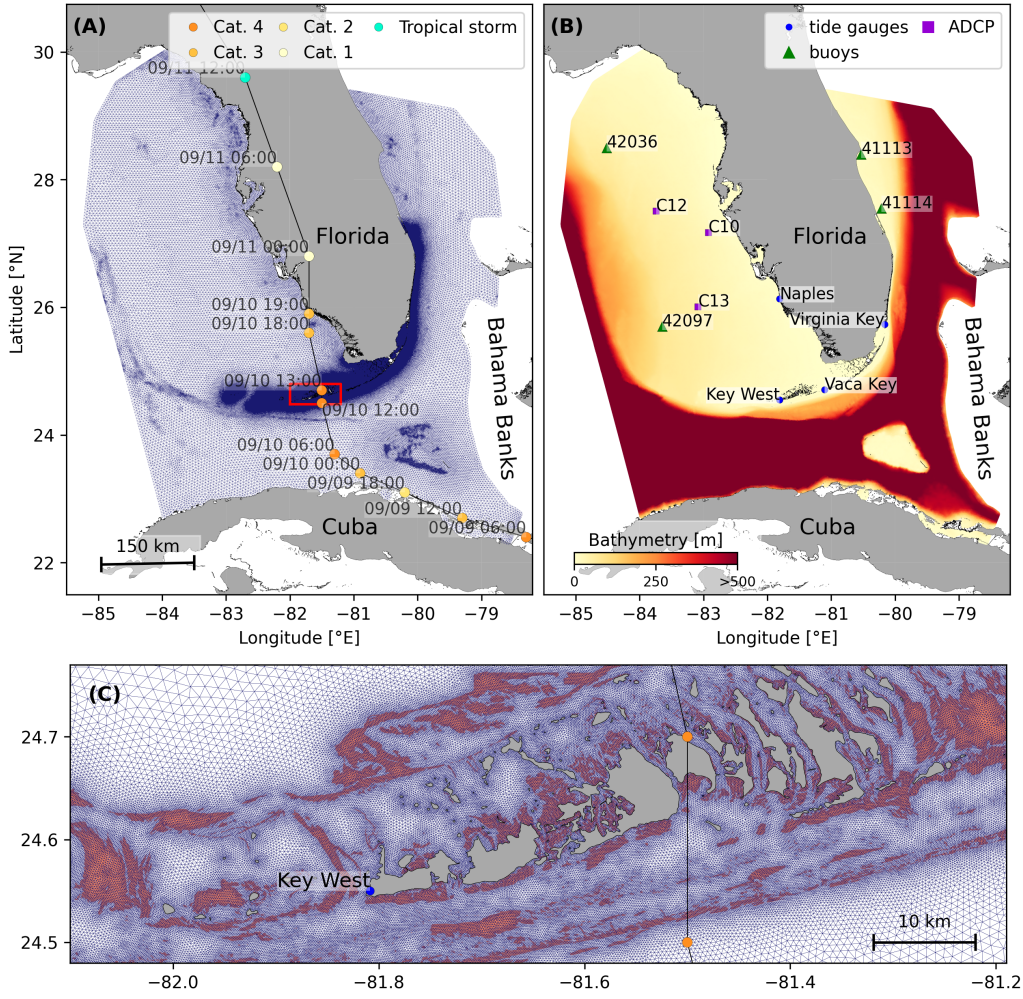


Fig. 1: (A) Mesh of the computational domain with the trajectory of Irma, category of the hurricane is given by the Saffir-Simpson color scale. (B) Bathymetry of the domain with the location of stations used for the validation of the model outputs. (C) Close up view of the Lower Keys area, where the mesh resolution reaches 100m near reefs (shown in dark orange) and islands (highlighted in dark grey)

wind profiles did not cover the whole model extent during the passage of the hurricane and were thus blended within coarser wind field extracted from ECMWF ERA-5 datasets (Fig. 2A). The pressure field during the passage of Hurricane Irma was also reconstructed using ERA-5 data. However, the coarse resolution of the dataset smoothes out the depression at the center of the hurricane, leading to an underestimation of the pressure gradient (Fig. 2B). To better capture the central depression of Irma, we therefore built a hybrid pressure field using the position and the minimal pressure of the core of the hurricane based on its track as recorded in the HURDAT 2 database (Landsea and Franklin, 2013). Based on this information, the hybrid pressure field was constructed by combining an idealized Holland pressure profile (Lin and Chavas, 2012) within the radius of maximum wind speed of Irma (Knaff et al., 2018) with ERA-5 pressure field. The transition from the Holland profile to ERA-5 data outside the radius of maximum wind speed data was performed using a smooth step function (Fig. 2).

2.3. Hydrodynamic model

Ocean currents generated during hurricane Irma around South Florida were modelled using the 2D barotropic version of the unstructured-mesh coastal ocean model SLIM¹. The model mesh covers an area similar to the model extent of Dobbelaere et al. (2020b), that includes the FRT but also the Florida Straits and part of the Gulf of Mexico (Figure 1). However, this area has been slightly extended northeastward and westward in order to include the NOAA-NDBC buoys. Furthermore, to withstand potential cell drying during the hurricane, we solved the conservative shallow water equations with

¹<https://www.slim-ocean.be>

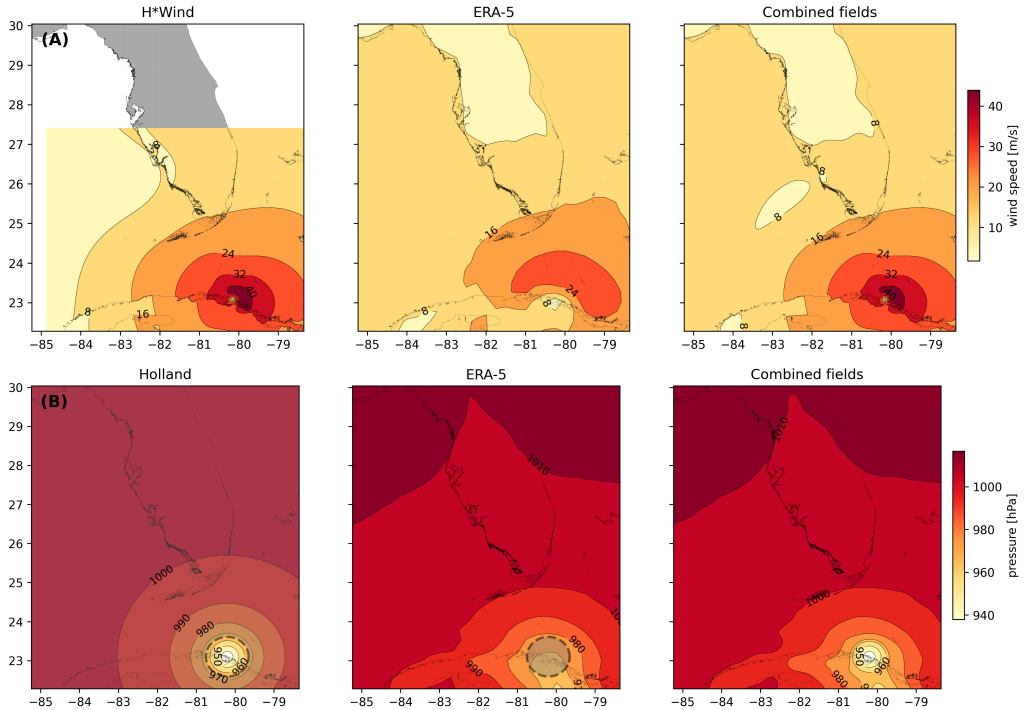


Fig. 2: Snapshot of the hybrid wind (A) and pressure (B) profiles constructed to capture the passage of Hurricane Irma at 1800 UTC on 9 September 2017. Wind profiles are obtained by combining high resolution H*Wind with coarser ERA-5 wind fields. The pressure field is built by combining the ERA-5 pressure field with an idealized Holland pressure profile based on the track of Irma in the HURDAT 2 database. Holland field was only used within the radius of maximum wind speed (dashed grey line) of the hurricane to capture its central depression.

₁₃₄ wetting-drying:

$$\begin{aligned} \frac{\partial H}{\partial t} + \nabla \cdot (\mathbf{U}) &= 0 , \\ \frac{\partial \mathbf{U}}{\partial t} + \nabla \cdot \left(\frac{\mathbf{U}\mathbf{U}}{H} \right) &= -f\mathbf{e}_z \times \mathbf{U} + \alpha g H \nabla(H - h) - \frac{1}{\rho} \nabla p_{\text{atm}} + \frac{1}{\rho} \boldsymbol{\tau}_s \quad (1) \\ &\quad + \nabla \cdot (\nu \nabla \mathbf{U}) - \frac{C_b}{H^2} |\mathbf{U}| \mathbf{U} + \gamma (\mathbf{U}_{\text{ref}} - \mathbf{U}) , \end{aligned}$$

₁₃₅ where H is the water column height and \mathbf{U} is the depth-averaged transport;
₁₃₆ f is the Coriolis coefficient; g is the gravitational acceleration; h is the
₁₃₇ bathymetry; α is a coefficient stating whether the mesh element is wet ($\alpha = 1$)
₁₃₈ or dry ($\alpha = 0$) (Le et al., 2020); ν is the viscosity; C_b is the bulk bottom drag
₁₃₉ coefficient; p_{atm} is the atmospheric pressure; $\boldsymbol{\tau}_s$ is the surface stress, usually
₁₄₀ due to wind; and γ is a relaxation coefficient towards a reference transport \mathbf{U}_{ref} .
₁₄₁ As in Frys et al. (2020) and Dobbelaere et al. (2020b), SLIM currents were
₁₄₂ gradually relaxed towards the operational Navy HYCOM product (GOMl0.04²,
₁₄₃ Chassignet et al. (2007)) in regions where the water depth exceeds 50m.

₁₄₄ At very high wind speeds, the white cap is blown off the crest of the
₁₄₅ waves. This phenomenon, also known as spumes, has been hypothesized to
₁₄₆ generate a layer of droplets that acts as a slip layer for the winds at the
₁₄₇ ocean-atmosphere interface (Holthuijsen et al., 2012). It causes a saturation
₁₄₈ of the wind drag coefficient for strong winds (Powell et al., 2003; Donelan
₁₄₉ et al., 2004; Curcic and Haus, 2020). We take this saturation effect into
₁₅₀ account by using the wind drag parameterization of Moon et al. (2007). In
₁₅₁ this parameterization, the drag coefficient C_d depends on the wind speed at
₁₅₂ 10-m height U_{10} according to:

$$C_d = \kappa^2 \log \left(\frac{10}{z_0} \right)^{-2} \quad (2)$$

²<https://www.hycom.org/data/goml0pt04>

153 where κ is the von Karman constant and z_0 is the roughness length expressed
 154 as:

$$z_0 = \begin{cases} \frac{0.0185}{g} U_*^2 & \text{if } U_{10} \leq 12.5 \text{ m/s ,} \\ [0.085(-0.56U_*^2 + 20.255U_*) + 2.458] - 0.58] \times 10^{-3} & \text{if } U_{10} > 12.5 \text{ m/s ,} \end{cases} \quad (3)$$

155 with U_* the friction velocity. The relation between U_{10} and U_* is given by:

$$U_{10} = -0.56U_*^2 + 20.255U_* + 2.458 . \quad (4)$$

156 The mesh resolution depends on the distance to the coastlines and reefs
 157 following the approach of Dobbelaere et al. (2020b). The mesh is then further
 158 refined according to bathymetry value and gradient, as suggested in the
 159 SWAN user-guide³. Such an approach improves the model efficiency as the
 160 mesh resolution is only increased where required by the currents and waves
 161 dynamics. The mesh was generated with the seamsh⁴ Python library, which is
 162 based on the open-source mesh generator GMSH (Geuzaine and Remacle,
 163 2009). It is composed of approximately 7.7×10^5 elements. The coarsest
 164 elements, far away from the FRT, has a characteristic length of about 5 km
 165 whereas the finest elements have a characteristic length of about 100 m along
 166 the coastlines and over the reefs (Fig 1).

167 2.4. Wave model

168 Waves were modelled using the parallel unstructured-mesh version of the
 169 Simulating WAves Nearshore (SWAN) model (Booij et al., 1999), one of the
 170 most popular wave models for coastal areas and inland waters. It solves the
 171 action balance equation (Mei, 1989):

$$\frac{\partial N}{\partial t} + \nabla_{\mathbf{x}} \cdot [(\mathbf{c}_g + \mathbf{u})N] + \frac{\partial}{\partial \theta}[c_\theta N] + \frac{\partial}{\partial \sigma}[c_\sigma N] = \frac{S_{in} + S_{ds} + S_{nl}}{\sigma} , \quad (5)$$

³<http://swanmodel.sourceforge.net/unswan/unswan.htm>

⁴<https://pypi.org/project/seamsh/>

where $N = E/\sigma$ is the wave action density and E is the wave energy spectrum; θ is the wave propagation direction; σ is the intrinsic wave frequency; \mathbf{c}_g is the wave group velocity, $\mathbf{u} = \mathbf{U}/H$ is SLIM depth-averaged current velocity; c_θ and c_σ are the propagation velocities in spectral space due to refraction and shifting in frequency due to variations in depth and currents; and S_{in} , S_{ds} , and S_{nl} respectively represent wave growth by wind, wave decay and nonlinear transfers of wave energy through interactions between triplets and quadruplets. The wave spectra were discretized with 48 direction bins and 50 frequency bins logarithmically distributed from 0.03 to 2 Hz. Exponential wind growth was parameterized using the formulation of Janssen (1991), while dissipations by whitecapping and bottom dissipations followed the formulations of Komen et al. (1984) and Madsen et al. (1989), respectively. Coefficients for exponential wind growth and whitecapping parameterizations were based on the results of Siadatmousavi et al. (2011), and significantly differ from SWAN's default settings. By default, SWAN implements the wind input formulation of Komen et al. (1984) and the steepness-dependent coefficient governing dissipation by whitecapping is a linear function of the wave number. In this study, this steepness-dependent coefficient is a quadratic function of the wave number, as it showed better predictions of the significant wave height in the study of Siadatmousavi et al. (2011). The choice of these formulations was motivated by the appearance of numerical instabilities in the region of the Gulf Stream when using SWAN's default parameter values. Finally, wave boundary conditions were derived from WAVEWATCH III (Tolman et al., 2009) spectral outputs at NDBC buoy locations. We selected these datasets as the large number of NDBC buoys around our region of interest allowed for a fine representation of the wave spectra on the boundary of the domain.

Surface waves induce a net drift in the direction of the wave propagation, known as the Stokes drift (Van Den Bremer and Breivik, 2018; Stokes, 1880). This net drift has a significant impact on sediment transport in

202 nearshore regions (Hoefel and Elgar, 2003), on the formation of Langmuir
 203 cells (Langmuir, 1938; Craik and Leibovich, 1976) as well as on the transport
 204 of heat, salt or pollutants such as oil or micro-plastic in the upper ocean layer
 205 (McWilliams and Sullivan, 2000; Röhrs et al., 2012; Drivdal et al., 2014). To
 206 correctly model the Stokes drift profile in mixed wind-driven sea and swell
 207 conditions, the full two-dimensional wave spectrum must be represented by a
 208 spectral wave model within a wave-current coupling (Van Den Bremer and
 209 Breivik, 2018). We therefore used SWAN modelled spectra to compute the
 210 Stokes drift as follows:

$$\mathbf{u}_s = \int_0^{2\pi} \int_0^{+\infty} \frac{\sigma^3}{h \tanh(2kh)} E(\sigma, \theta) (\cos \theta, \sin \theta) d\sigma d\theta , \quad (6)$$

211 where k is the norm of the wave vector; h is the water depth; and $E(\sigma, \theta)$ is
 212 the wave energy density.

213 *2.5. Coupled model*

214 SLIM and SWAN are coupled so that they run on the same computational
 215 core and the same unstructured mesh. SLIM is run first and passes the
 216 wind velocity (\mathbf{U}_{10}), water level ($\eta = H - h$) and depth-averaged current
 217 ($\mathbf{u} = \mathbf{U}/H$) fields to SWAN, as well as a roughness length (z_0) for the bottom
 218 dissipation formulation of Madsen et al. (1989). This roughness length is
 219 computed from SLIM's bulk drag coefficient C_b following the approach of
 220 Dietrich et al. (2011) so that both models have consistent bottom dissipation
 221 parameterizations. SWAN then uses these quantities to compute the wave
 222 radiation stress gradient, that is then passed to SLIM as the force exerted
 223 by waves on currents $\boldsymbol{\tau}_{\text{wave}}$ (Fig. 3). SLIM then uses this quantity to
 224 update the value of the surface stress $\boldsymbol{\tau}_s$ in Eq. (1), that now becomes
 225 the sum of wind and wave-induced stresses $\boldsymbol{\tau}_s = \boldsymbol{\tau}_{\text{wind}} + \boldsymbol{\tau}_{\text{wave}}$. Here, the
 226 momentum flux from the atmosphere to the ocean is taken as the commonly-
 227 used full wind stress $\boldsymbol{\tau}_{\text{wind}}$. Doing so, we neglect the momentum advected
 228 away from the storm by the waves, leading to a 10-15% overestimation of the

momentum flux in hurricane winds (Curcic, 2015). Moreover, we followed the approach of Dietrich et al. (2012) by characterizing the wave-induced stresses using the radiation-stress representation instead of the vortex-force representation (McWilliams et al., 2004). Although the later provides a clearer and more meaningful decomposition of the wave effect, we implemented the first representation for the sake of simplicity as it allows us to provide the whole wave contribution as an additional surface stress to SLIM (Lane et al., 2007).

SLIM’s governing equations are integrated using an implicit time integration scheme while SWAN is unconditionally stable (Dietrich et al., 2012), allowing both models to be run with relatively large time steps. In this study, the stationary version of SWAN was used, *i.e.* the time derivative of Eq. 5 was set to zero. This resulted in reduced scaling and convergence rates than with the nonstationary version of SWAN but increased the stability of the model. The wave spectra at each node of the mesh was saved at the end of each iteration to serve as initial conditions for the next one. Both models were run sequentially using a time step of 600 s, so that each computational core was alternatively running either SLIM or SWAN. As in the coupling between SWAN and ADCIRC (Dietrich et al., 2012), both models use the same local sub-mesh, allowing for a one-to-one correspondence between the geographic locations of the mesh vertices. No interpolation is therefore needed when passing the discretised variables from one model to the other, which allows an efficient inter-model communication. However, as SLIM is based on a discontinuous Galerkin finite element method, an additional conversion step to a continuous framework was required to transfer SLIM nodal quantities to SWAN.

2.6. Quantifying the effect of wave-current interactions on transport

To quantify the impact of wave-current interactions on transport processes, we compared the trajectories of passive particles advected by the uncoupled SLIM and coupled SLIM+SWAN currents during the passage of Irma in the

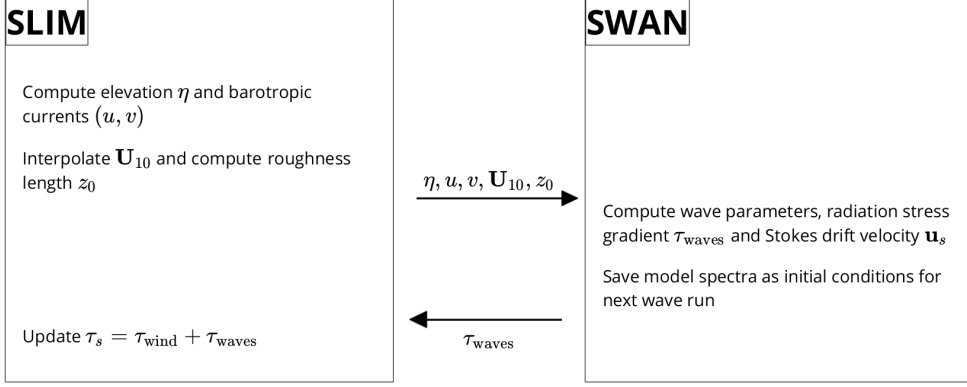


Fig. 3: Schematic illustration of the coupled SLIM+SWAN model.

259 Lower Keys. Furthermore, the depth-averaged Stokes drift was computed
 260 using the wave spectra of the coupled model SLIM+SWAN run as well as
 261 those of an uncoupled SWAN run. Particles were released on the inner and
 262 outer shelves at the points highlighted by red and blue dots in Fig. 4 on
 263 Sept. 7 at 0000 UTC and then tracked until Sept. 15. These initial particle
 264 positions were found using backtracking methods (Dobbelare et al., 2020a)
 265 to ensure that the release particles would intersect the path of Irma during
 266 its passage through the Florida Keys. We first defined two 25 km^2 circular
 267 regions on the trajectory of the hurricane (see red and blue circles in Fig. 4).
 268 Particles within these two regions were then tracked backward in time using
 269 uncoupled SLIM currents from the exact time of the passage of the hurricane
 270 until Sept. 7 at 0000 UTC. Their positions at the end of the backward
 271 simulation (see red and blue particle clouds in Fig. 4) corresponds to the
 272 initial condition of the forward transport simulations described below. We
 273 then compared the trajectories of particles originating from these regions and
 274 advected forward in time by different sets of currents: (i) uncoupled SLIM
 275 currents alone; (ii) coupled SLIM+SWAN currents; (iii) SLIM currents with
 276 the addition of the depth-averaged Stokes drift computed with the coupled
 277 wave-current model (Stokes-C); (iv) SLIM+SWAN currents with Stokes-C;

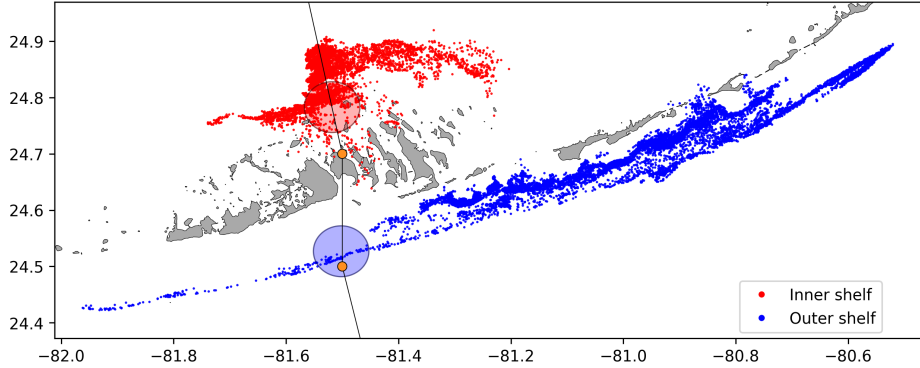


Fig. 4: Release regions of the passive particles on the inner and outer shelves (red and blue clouds) obtained by backtracking particles released in the red and blue circular areas during the passage of Irma.

and (v) SLIM currents with the depth-averaged Stokes drift computed with the uncoupled wave model (Stokes-U). Particles trajectories are compared by computing the distances between the centers of mass of the particle clouds through time.

3. Results

We first validated the reconstructed atmospheric fields of hurricane Irma as well as the outputs of our coupled wave-current model against field measurements. A summary of the error statistics is given in Table 1. We then used the validated model outputs to simulate the transport of passive drifters in the Lower Keys during the passage of Hurricane Irma. These drifters were advected by the sets of currents described in section 2.6 and their trajectories were compared to evaluate the impact of the wave-current interactions and the Stokes drift on the transport processes during the passage of Irma.

3.1. Model validation

H*Wind winds and hybrid pressure field agree well with station measurements at Vaca Key station (Fig. 5). The hybrid pressure field shows a

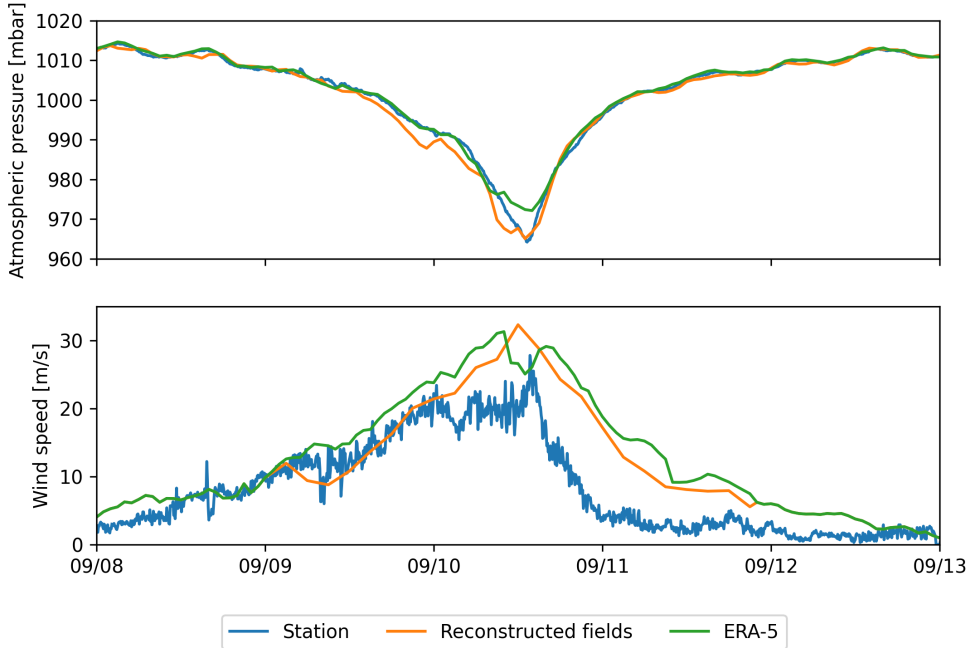


Fig. 5: Comparison of reconstructed wind atmospheric pressure with field measurements and coarser ECMWF ERA-5 profiles at Vaca Key station. The generated hybrid atmospheric forcings better reproduce the observed storm depression while H*wind winds better reproduce the measured peak in wind speed.

better agreement with observations than ERA-5 pressure as it successfully reproduces the storm depression. ERA-5 fields, on the other hand, fail to reproduce the low pressure at the core of the hurricane due to their coarser grid, leading to an overestimation of 8 mbar of the storm depression. Both H*Wind and ERA-5 agree well with observed wind speeds although both data sets tend to slightly overestimate the width and intensity of the wind peak. However, H*wind profiles better reproduce the timing of the observed peak, as ERA-5 winds tend to anticipate it. H*wind also exhibits a slightly narrower peak in wind speed, which better agrees with observations.

Hydrodynamic outputs of the coupled wave-current model agree well with tide gauge (Fig. 6) and ADCP measurements (Fig. 7). Despite a slight overestimation of the amplitude of sea surface elevation (Table 1) in fair

306 weather conditions, the timing and amplitude of the storm surges are well
307 reproduced by the coupled model. The largest model error during the surge
308 is an overestimation of 18 cm of the elevation peak at Virginia Key. The fit is
309 especially good at Naples, where both the large positive and negative surges
310 are captured by the coupled model with an error of less than 5 cm. Modelled
311 2D currents were validated against depth-averaged ADCP measurements
312 at mooring stations C10, C12 and C13 (Fig. 7). As in Liu et al. (2020),
313 we performed the vector correlation analysis of Kundu (1976) to compare
314 modelled and observed current velocity vectors. Correlation coefficients (ρ)
315 between simulated and observed depth-averaged currents are 0.84, 0.74 and
316 0.73 at stations C10, C12 and C13, respectively. Average veering angles were
317 computed as well and are below 12°, as in (Liu et al., 2020). Furthermore, our
318 model tends to produce larger prediction errors on the northward component
319 of the depth-averaged currents than the eastward one (Table 1). [replace
320 by summary of information of Table] As expected from a depth-averaged
321 model, the best fit with observations is obtained at the shallowest mooring
322 C10, located on the 25 m isobath, with an average veering angle of 6° and
323 smaller error statistics (Table 1).

324 The simulated significant wave height agrees well with observations on
325 the WFS, where errors on the peak value do not exceed 5% (Fig. 8). On
326 Florida's eastern shelf, errors are slightly larger and reach 20%. Although the
327 model outputs agree well with observations, a lag in significant wave height is
328 observed for all 4 buoys. Moreover, the peak in significant wave height tends
329 to be underestimated at buoys 41113 and 41114, located on the East Florida
330 Shelf. Other wave parameters were better reproduced by the model on the
331 WFS as well (see buoy 42036 in Fig. 8 and Table 1).

332 *3.2. Impact of waves on currents and transport*

333 We evaluated the impact of wave-current interactions on modelled currents
334 during the passage of Irma in the Lower Keys, between Sept. 7 and 13, 2017.
335 First, we computed the maximum difference between currents modelled by

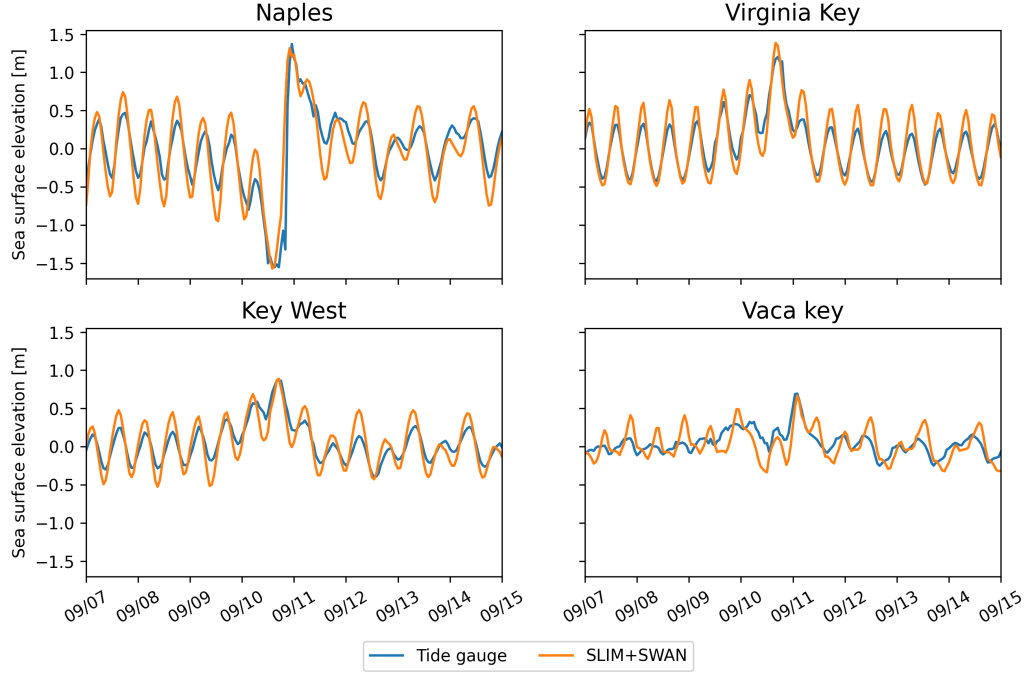


Fig. 6: Comparison of modelled sea surface elevation at the 4 tide gauges shown in Fig. 1B. The timing and amplitudes of the storm surges are well reproduced by the model

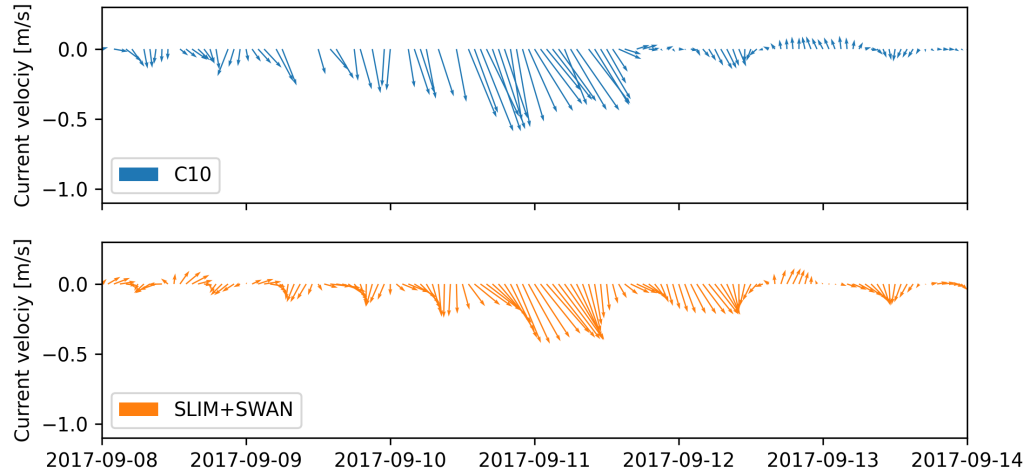


Fig. 7: Comparison of modelled current velocity with observed velocity at mooring C10 (see Fig. 1B for its location). Modelled current velocities agree well with observations, with a correlation coefficient of 0.83 and an average veering angle of 6°.

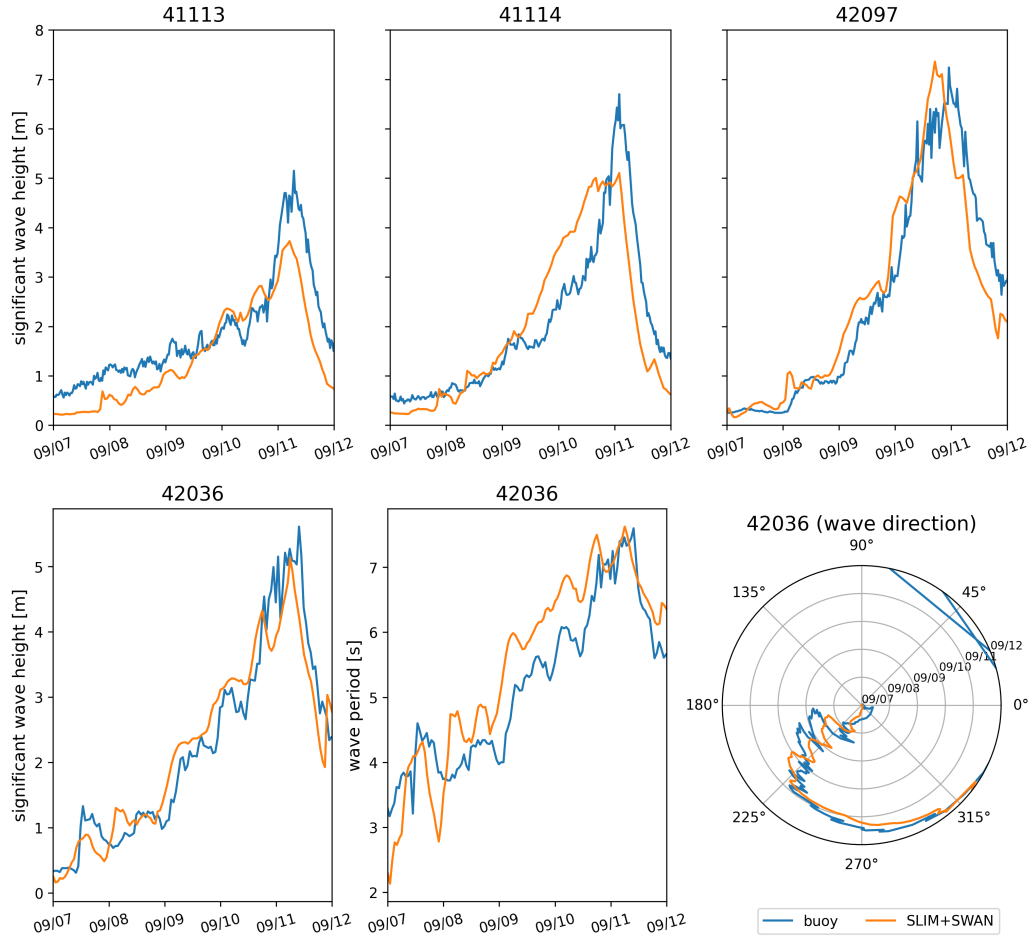


Fig. 8: Comparison of modelled wave parameters with observation at the 4 buoys location (locations shown in Fig. 1B). Modelled significant wave height agrees well with field measurement.

Station	Variable	Bias	MAE	RMSE
Vaca Key	sse (m)	n/a	0.12	0.16
	U_{10} (m/s)	1.51	1.85	2.61
	p_{atm} (hPa)	-0.21	0.59	1.03
Key West	sse (m)	n/a	0.11	0.13
Virginia Key	sse (m)	n/a	0.10	0.13
Naples	sse (m)	n/a	0.18	0.23
C10	u (m/s)	-0.006	0.04	0.05
	v (m/s)	0.02	0.06	0.08
C12	u (m/s)	-0.01	0.06	0.07
	v (m/s)	0.06	0.09	0.11
C13	u (m/s)	0.004	0.06	0.08
	v (m/s)	0.04	0.06	0.08
41113	H_s (m)	-0.35	0.40	0.51
	T_m (s)	-2.18	2.47	3.13
41114	H_s (m)	-0.21	0.53	0.68
	T_m (s)	-1.69	2.53	3.15
42036	H_s (m)	-0.03	0.26	0.36
	T_m (s)	0.04	0.65	0.77
42097	H_s (m)	-0.15	0.40	0.57
	T_m (s)	0.02	0.62	0.74

Table 1: Error statistics comparing SLIM+SWAN simulated quantities with the measured sea surface elevation (sse), eastward and northward depth-average current velocities (u,v), significant wave height (H_s), and zero-crossing mean wave period (T_m). Model bias, mean absolute error (MAE), and root mean squared error (RMSE) are listed by variable (unit) and value.

336 SLIM and SLIM+SWAN during this period (Fig. 9A). The largest differences
337 in current speed were observed over the reefs, on the shelf break and around
338 islands. They can locally reach 1 m/s, with the coupled SLIM+SWAN model
339 yielding the largest amplitudes. The regions where the differences are the
340 largest experience the strongest radiation-stress gradient τ_{wave} (Fig. 9B)
341 induced by wave energy dissipation on the shelf-break and rough seabed
342 induce variations of the wave radiation stress (Longuet-Higgins and Stewart,
343 1964). This highlights the important protective role of the barrier formed
344 by the offshore reefs, that require a fine spatial resolution to be accurately
345 captured. Wave-induced differences in current speed were amplified by the
346 action of the wind stress τ_{wind} (Fig. 9C). Wind speeds were larger in the front
347 right quadrant of the hurricane (Zedler et al., 2009), yielding larger differences
348 on the right-hand side of the storm trajectory. This is especially clear in the
349 area between the Florida Keys and the Everglades, where relatively small
350 values of τ_{wave} nonetheless produce current speed differences of up to 0.5 m/s
351 because of the wind stress.

352 Waves play a significant role on the transport processes during and after
353 the passage of hurricane Irma (Fig. 10A). Comparing SLIM and SLIM+SWAN
354 shows that wave-current interactions alone yield differences of up to 5 km
355 between the modelled trajectories on the passage of the hurricane. These
356 differences exceed 10 km on the outer shelf when Stokes drift is taken into
357 account. The impact of the waves on the transport processes differs signifi-
358 cantly between the inner and outer shelves, with wave-induced differences in
359 trajectories 4 to 5 times larger on the outer shelf. Furthermore, the distances
360 between the centers of mass of the clouds of particles tend to stabilize on
361 the inner shelf after the passage of Irma, while they keep increasing on the
362 other shelf up to two days after the passage of the hurricane when taking
363 Stokes drift into account. These distances then stabilize for about a day
364 before they start decreasing (see right panel of Fig. 10A). However, when
365 considering wave-current interactions alone (SLIM vs. SLIM+SWAN), the

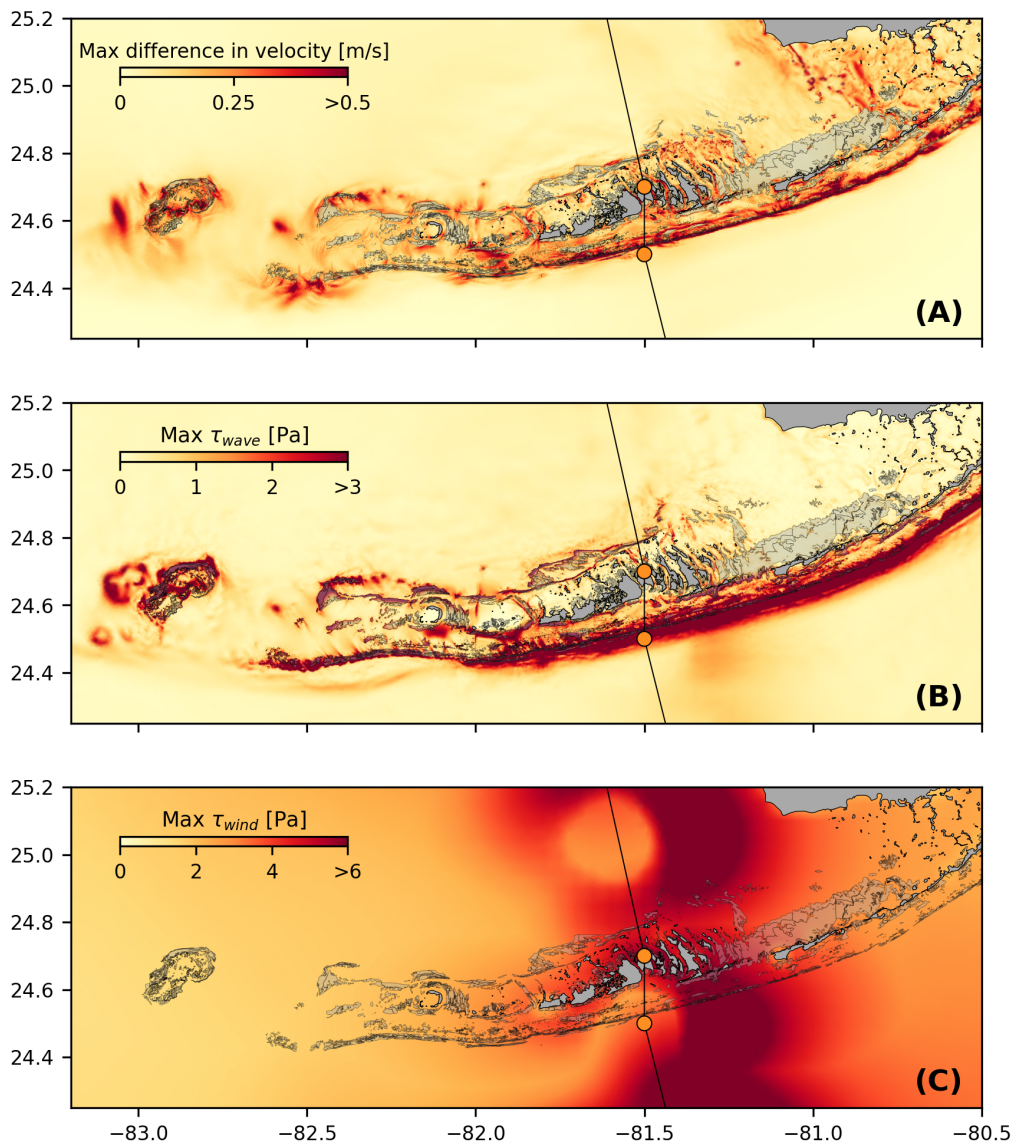


Fig. 9: (A). Maximum difference between SLIM and SLIM+SWAN currents during the passage of Irma in the Lower Florida Keys; (B) Maximum wave radiation stress gradient τ_{wave} and (C) maximum wind stress τ_{wind} (C) generated by the hurricane. Radiation stress gradient yields difference larger than 0.5 m/s in current velocities, especially over offshore reefs.

366 distance between the clouds of particles starts to decrease just after the
367 passage of Irma.

368 The Stokes drift appears to have a larger effect than the radiation stress
369 gradient and the wave-current interactions (Fig 10A). Nonetheless, comparing
370 the different curves for the outer shelf suggests that the radiation-stress
371 gradient induces effects similar to the impact of the Stokes drift in this region
372 during the passage of Irma. However, comparing SLIM and SLIM+SWAN
373 both on the inner and other shelf, we see that this impact is negligible during
374 the rest of the simulation. Moreover, comparison of Stokes-U and Stokes-C
375 (Fig. 10B) indicates that the difference between the trajectories of particles
376 advected by the two Stokes drift do not exceed 2 km, with larger discrepancies
377 on the outer shelf. The sudden increase of 'SLIM+Stokes-C vs SLIM+Stokes-
378 U' curves on the passage of Irma (and two days after on the outer shelf) and
379 their stabilization afterwards suggest that taking wave-currents interactions
380 into account when modeling waves mostly has an impact during (and directly
381 after) the passage of the hurricane.

382 4. Discussion

383 Our results show that neglecting wave effects can induce differences of up
384 to 1 m/s in modelled current velocities, leading to variations of more than 10
385 km in modelled trajectories. These differences in modelled trajectories were
386 significantly larger and required more time to stabilize on the outer shelf. The
387 impact of the Stokes drift dominates the effects of wave-current interactions
388 through the radiation stress gradient, except at the moment of the passage
389 of the hurricane, when both contributions are similar. Finally, neglecting
390 wave-current interactions when computing Stokes drift lead to variations of
391 up to 2 km in modelled trajectories on the passage of the hurricane.

392 Despite slightly overestimating the amplitude of the sea surface elevation
393 in fair weather conditions, the coupled model reproduces correctly the timing
394 and amplitude of the observed storm surge (Fig. 6). All elevation peaks are

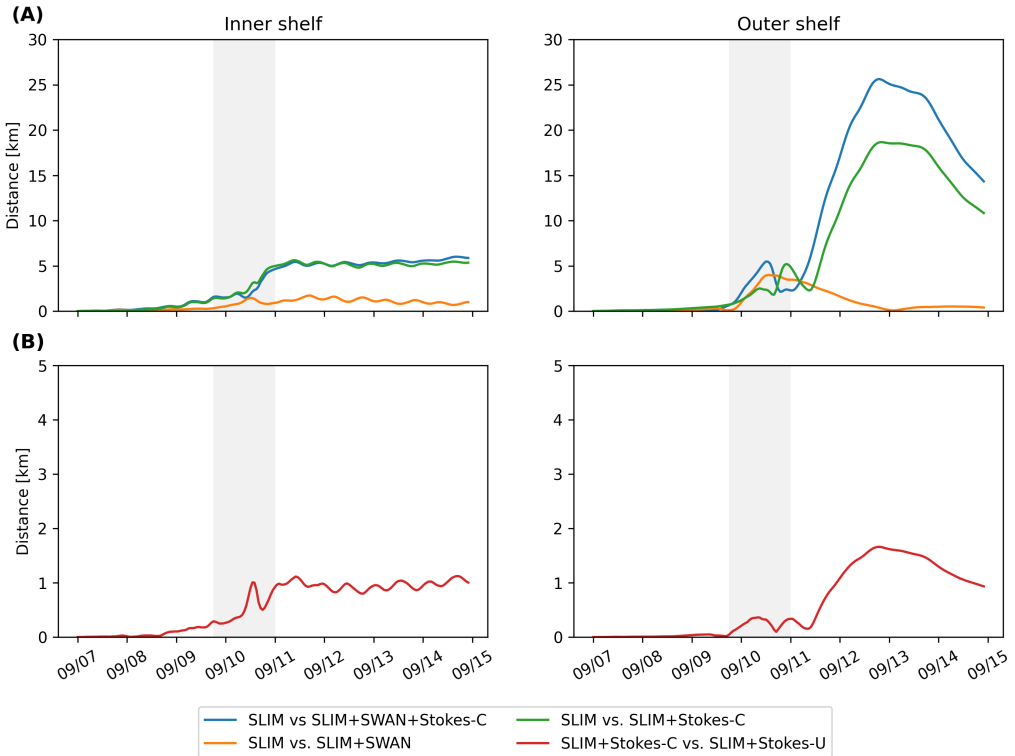


Fig. 10: Difference between the centers of mass of the particle clouds released from the regions highlighted in Fig. 4 and advected by different combinations of coupled and uncoupled velocity fields. **Matthieu:** prsenter plus d'informations sur la Figure 8, notamment les nuages de points issus des deux simulations (SLIM et SLIM+SWAN+Stokes-C), ainsi que les centres de masses correspondants. Ca devrait permettre de soutenir la partie rsultats.

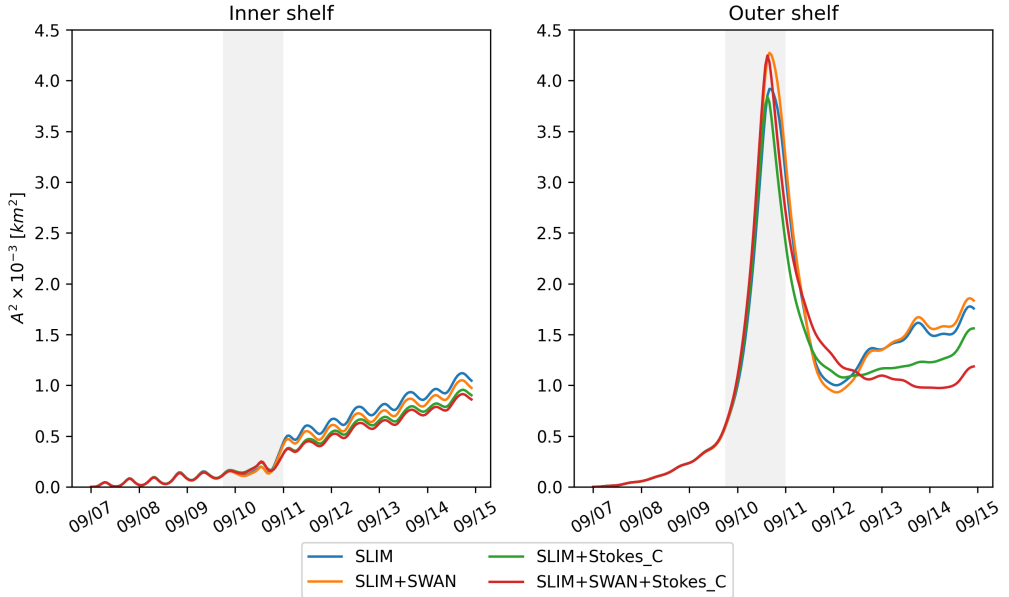


Fig. 11: Dispersion of particles with different velocity fields → not sure to know what to say about that...

395 captured with a 4% accuracy at every stations except Virginia key, where the
 396 surge was overestimated by about 15%. Such accuracy is key to predict the
 397 damages caused by the hurricane, as most destroyed and severely damaged
 398 buildings in the Florida keys during Hurricane Irma were caused by storm
 399 surge and waves (Xian et al., 2018). Furthermore, the high resolution of
 400 model in the regions captures flow accelerations between islands and reefs,
 401 allowing for a precise representation of the surge risk in the Florida Keys. In
 402 addition to accurately capture positive surges, the model also reproduced the
 403 observed negative surge in Naples with an error of about 1%. This result is
 404 of interest from a biological point of view as negative surges, although less
 405 studied, affect water exchanges between the estuaries and the coastal ocean
 406 and disturb the benthic ecosystems (Liu et al., 2020). Such rapid decrease
 407 in water level followed by a positive surge cause massive freshwater inflows,
 408 generating a significant decrease in water salinity (Wachnicka et al., 2019).

409 Strong currents such as the Gulf Stream affect waves through refraction
410 over gradients in current velocity, shoaling and breaking of opposing waves
411 or lengthening of following waves (Hegermiller et al., 2019). Under hurri-
412 cane conditions, these interactions can cause numerical instabilities in the
413 wave model if appropriate parameterizations and model resolution are not
414 applied. Hegermiller et al. (2019), for instance, used a 5-km model grid and
415 48 directional bins to capture spatial gradients in wave height induced by
416 wave-currents interactions in the Gulf Stream during Hurricane Matthew
417 (2016). These guidelines were followed when defining the coarsest resolution of
418 the model mesh as well as the spectral discretization of SWAN. Boundary con-
419 ditions and directional spreading of the incident waves also play a significant
420 role when modeling wave-current interactions at meso- and submesoscales
421 (Villas Bôas et al., 2020), which motivated our choice of imposing full spectra
422 on the boundary of the wave model instead of bulk parameters. Finally,
423 SWAN default parameterizations for wind energy input and whitecapping
424 caused numerical instabilities by overestimating wave growth and steepness
425 on the boundary of the Gulf Stream on the passage of Irma. This overes-
426 timation was solved by using the parameterization of Siadatmousavi et al.
427 (2011). The parameters used in this study were calibrated on the Northern
428 Gulf of Mexico, which might explains that our model better reproduces wave
429 parameters at buoys 42036 and 4207, located on the WFS. However, these
430 calibrated parameters might underestimate wind-induced wave growth might
431 underestimate Florida's eastern shelf. Consequently, incident wave do not
432 receive enough energy to grow after breaking on the bank boundary, leading
433 to the underestimation of the significant wave height at buoys 41113 and
434 41114. A more extensive calibration study might therefore be necessary to
435 achieve good agreement with field measurements on both sides of Florida.
436 Nonetheless, as this study focuses on the wave produced by Irma, which
437 made landfall on the western coasts of Florida, the use of parameterizations
438 calibrated for the Gulf of Mexico seems reasonable.

439 Wave impact during Irma is different on the inner and outer shelves. It is
440 less important on the inner shelf because of the sheltering of the inner shelf
441 due to reefs and islands as well as wave breaking on the shelf break. The inner
442 shelf hence experiences weaker waves and currents, inducing weaker and more
443 localized transport. Furthermore, the impact of winds on waves is reduced
444 in shallower areas under the action of depth-induced breaking. This might
445 explain why differences between particle trajectories stabilize on the inner
446 shelf just after the passage of Hurricane Irma. However, the Florida Keys
447 still experienced strong winds after the passage of the core of the hurricane,
448 which generated high waves in the deeper areas. This might explain why the
449 differences on between the modelled trajectories kept increasing on the outer
450 shelf under the action of strong Stokes drift up to two days after the passage
451 of the hurricane.

452 The distance between the centers of mass of clouds of particles coupled and
453 uncoupled Stokes drift did not exceed 2 km (Fig. 10). This suggest that taking
454 wave-currents interactions into account when computing Stokes drift, even
455 under hurricane conditions yields a limited impact. Furthermore, combining
456 the coupled Stokes drift with the coupled and uncoupled SLIM currents
457 produced similar trajectories on the inner shelf, which seems to indicate that
458 wave impact of currents is limited in this region. This would suggest that it is
459 not necessary to take wave-current interactions into account when modeling
460 the trajectories of tracers in shallow, sheltered areas such as the inner WFS
461 during a hurricane. Uncoupled currents with uncoupled Stokes drift should
462 give a reasonably accurate approximation of the transport processes. However,
463 this does not hold for deeper regions, as highlighted by the differences between
464 'SLIM vs. SLIM+SWAN+Stokes-C' and 'SLIM+Stokes-C' in the outer shelf.

465 5. Conclusion

466 We developed a coupled wave-current model to study the impact of
467 waves on transport processes during Hurricane Irma. In order to accurately

468 represent the wind and pressure profiles of the hurricane, we built hybrid fields
469 by combining coarser ERA-5 data with high-resolution H*Wind data for
470 the wind speed and idealized Holland profiles for the pressure. Comparing
471 these hybrid profiles with field observations showed that they were better at
472 reproducing the observed central depression of the hurricane as well as the
473 peak in wind speed than ERA-5 data. Using these hybrid fields as forcings,
474 our coupled model accurately reproduced the storm surge at NDBC buoy
475 locations and produced currents and wave parameters in good agreement
476 with field observations, especially on the WFS. The modelled currents and
477 Stokes drift were then used to evaluate the impact of waves on the trajectory
478 of passive drifters on the passage of the hurricane through the Florida Keys.

479 [limitations of model]

480 Wave coupling needs to be taken into account during heavy-wind events
481 but not necessarily in milder conditions. While the wave-current interaction
482 plays an important role and can lead to differences of up to..., the Stokes
483 drift is about ... more intense and should thus be considered in priority

484 **Acknowledgments**

485 Computational resources were provided by the Consortium des Équipements
486 de Calcul Intensif (CÉCI), funded by the F.R.S.-FNRS under Grant No.
487 2.5020.11. Thomas Dobbelaere is a PhD student supported by the Fund for
488 Research training in Industry and Agriculture (FRIA/FNRS).

489 **References**

- 490 Bever, A.J., MacWilliams, M.L., 2013. Simulating sediment transport pro-
491 cesses in San Pablo Bay using coupled hydrodynamic, wave, and sediment
492 transport models. Marine Geology 345, 235–253.
- 493 Bhatia, K.T., Vecchi, G.A., Knutson, T.R., Murakami, H., Kossin, J., Dixon,
494 K.W., Whitlock, C.E., 2019. Recent increases in tropical cyclone intensifi-
495 cation rates. Nature Communications 10, 1–9.

- 496 Booij, N., Ris, R.C., Holthuijsen, L.H., 1999. A third-generation wave
497 model for coastal regions: 1. Model description and validation. *Journal of*
498 *Geophysical Research: Oceans* 104, 7649–7666.
- 499 Breivik, Ø., Allen, A.A., Maisondieu, C., Olagnon, M., 2013. Advances in
500 search and rescue at sea. *Ocean Dynamics* 63, 83–88.
- 501 Chassignet, E.P., Hurlburt, H.E., Smedstad, O.M., Halliwell, G.R., Hogan,
502 P.J., Wallcraft, A.J., Baraille, R., Bleck, R., 2007. The HYCOM (hybrid
503 coordinate ocean model) data assimilative system. *Journal of Marine*
504 *Systems* 65, 60–83.
- 505 Chen, C., Huang, H., Beardsley, R.C., Liu, H., Xu, Q., Cowles, G., 2007.
506 A finite volume numerical approach for coastal ocean circulation studies:
507 Comparisons with finite difference models. *Journal of Geophysical Research:*
508 *Oceans* 112.
- 509 Craik, A.D., Leibovich, S., 1976. A rational model for Langmuir circulations.
510 *Journal of Fluid Mechanics* 73, 401–426.
- 511 Curcic, M., 2015. Explicit air-sea momentum exchange in coupled atmosphere-
512 wave-ocean modeling of tropical cyclones. Ph.D. thesis.
- 513 Curcic, M., Chen, S.S., Özgökmen, T.M., 2016. Hurricane-induced ocean
514 waves and stokes drift and their impacts on surface transport and dispersion
515 in the Gulf of Mexico. *Geophysical Research Letters* 43, 2773–2781.
- 516 Curcic, M., Haus, B.K., 2020. Revised estimates of ocean surface drag in
517 strong winds. *Geophysical Research Letters* 47, e2020GL087647.
- 518 Dietrich, J., Bunya, S., Westerink, J., Ebersole, B., Smith, J., Atkinson,
519 J., Jensen, R., Resio, D., Luettich, R., Dawson, C., et al., 2010. A high-
520 resolution coupled riverine flow, tide, wind, wind wave, and storm surge
521 model for southern Louisiana and Mississippi. Part II: Synoptic description

- 522 and analysis of Hurricanes Katrina and Rita. Monthly Weather Review
523 138, 378–404.
- 524 Dietrich, J., Westerink, J., Kennedy, A., Smith, J., Jensen, R., Zijlema, M.,
525 Holthuijsen, L., Dawson, C., Luettich, R., Powell, M., et al., 2011. Hurricane
526 Gustav (2008) waves and storm surge: Hindcast, synoptic analysis, and
527 validation in southern Louisiana. Monthly Weather Review 139, 2488–2522.
- 528 Dietrich, J.C., Tanaka, S., Westerink, J.J., Dawson, C., Luettich, R., Zijlema,
529 M., Holthuijsen, L.H., Smith, J., Westerink, L., Westerink, H., 2012. Per-
530 formance of the unstructured-mesh, SWAN+ ADCIRC model in computing
531 hurricane waves and surge. Journal of Scientific Computing 52, 468–497.
- 532 Dobbelaere, T., Muller, E., Gramer, L., Holstein, D., Hanert, E., 2020a.
533 Report on the potential origin of the SCTLD in the Florida Reef Tract.
534 Available online at: [https://floridadep.gov/rcp/coral/documents/
535 report-potential-origin-sctld-florida-reef-tract](https://floridadep.gov/rcp/coral/documents/report-potential-origin-sctld-florida-reef-tract).
- 536 Dobbelaere, T., Muller, E.M., Gramer, L.J., Holstein, D.M., Hanert, E., 2020b.
537 Coupled epidemic-hydrodynamic modeling to understand the spread of a
538 deadly coral disease in Florida. Frontiers in Marine Science 7, 1016.
- 539 Donelan, M., Haus, B., Reul, N., Plant, W., Stiassnie, M., Gruber, H., Brown,
540 O., Saltzman, E., 2004. On the limiting aerodynamic roughness of the
541 ocean in very strong winds. Geophysical Research Letters 31.
- 542 Drivdal, M., Broström, G., Christensen, K., 2014. Wave-induced mixing and
543 transport of buoyant particles: Application to the Statfjord A oil spill.
544 Ocean Science 10, 977–991.
- 545 Figueiredo, J., Baird, A.H., Connolly, S.R., 2013. Synthesizing larval com-
546 petence dynamics and reef-scale retention reveals a high potential for
547 self-recruitment in corals. Ecology 94, 650–659.

- 548 Frys, C., Saint-Amand, A., Le Hénaff, M., Figueiredo, J., Kuba, A., Walker,
549 B., Lambrechts, J., Vallaeyns, V., Vincent, D., Hanert, E., 2020. Fine-scale
550 coral connectivity pathways in the Florida Reef Tract: Implications for
551 conservation and restoration. *Frontiers in Marine Science* 7, 312.
- 552 Geuzaine, C., Remacle, J.F., 2009. Gmsh: A 3-d finite element mesh generator
553 with built-in pre-and post-processing facilities. *International journal for
554 numerical methods in engineering* 79, 1309–1331.
- 555 Harper, B., Kepert, J., Ginger, J., 2010. Guidelines for converting between
556 various wind averaging periods in tropical cyclone conditions.
- 557 Hegermiller, C.A., Warner, J.C., Olabarrieta, M., Sherwood, C.R., 2019.
558 Wave-current interaction between Hurricane Matthew wave fields and the
559 Gulf Stream. *Journal of Physical Oceanography* 49, 2883–2900.
- 560 Hoefel, F., Elgar, S., 2003. Wave-induced sediment transport and sandbar
561 migration. *Science* 299, 1885–1887.
- 562 Holthuijsen, L.H., Powell, M.D., Pietrzak, J.D., 2012. Wind and waves in
563 extreme hurricanes. *Journal of Geophysical Research: Oceans* 117.
- 564 Janssen, P.A., 1991. Quasi-linear theory of wind-wave generation applied to
565 wave forecasting. *Journal of Physical Oceanography* 21, 1631–1642.
- 566 Johns, W.E., Schott, F., 1987. Meandering and transport variations of the
567 Florida Current. *Journal of Physical Oceanography* 17, 1128–1147.
- 568 Knaff, J.A., Sampson, C.R., Musgrave, K.D., 2018. Statistical tropical cyclone
569 wind radii prediction using climatology and persistence: Updates for the
570 western North Pacific. *Weather and Forecasting* 33, 1093–1098.
- 571 Knutson, T., Camargo, S.J., Chan, J.C., Emanuel, K., Ho, C.H., Kossin, J.,
572 Mohapatra, M., Satoh, M., Sugi, M., Walsh, K., et al., 2020. Tropical
573 cyclones and climate change assessment: Part ii: Projected response to

- 574 anthropogenic warming. *Bulletin of the American Meteorological Society*
575 101, E303–E322.
- 576 Komen, G., Hasselmann, S., Hasselmann, K., 1984. On the existence of a
577 fully developed wind-sea spectrum. *Journal of Physical Oceanography* 14,
578 1271–1285.
- 579 Kossin, J.P., Knapp, K.R., Olander, T.L., Velden, C.S., 2020. Global increase
580 in major tropical cyclone exceedance probability over the past four decades.
581 *Proceedings of the National Academy of Sciences* 117, 11975–11980.
- 582 Kourafalou, V.H., Kang, H., 2012. Florida Current meandering and evo-
583 lution of cyclonic eddies along the Florida Keys Reef Tract: Are they
584 interconnected? *Journal of Geophysical Research: Oceans* 117.
- 585 Kundu, P.K., 1976. Ekman veering observed near the ocean bottom. *Journal*
586 *of Physical Oceanography* 6, 238–242.
- 587 Landsea, C.W., Franklin, J.L., 2013. Atlantic hurricane database uncertainty
588 and presentation of a new database format. *Monthly Weather Review* 141,
589 3576–3592.
- 590 Lane, E.M., Restrepo, J., McWilliams, J.C., 2007. Wave-current interaction:
591 A comparison of radiation-stress and vortex-force representations. *Journal*
592 *of physical oceanography* 37, 1122–1141.
- 593 Langmuir, I., 1938. Surface motion of water induced by wind. *Science* 87,
594 119–123.
- 595 Le, H.A., Lambrechts, J., Ortleb, S., Gratiot, N., Deleersnijder, E., Soares-
596 Frazão, S., 2020. An implicit wetting–drying algorithm for the discontinuous
597 galerkin method: application to the tonle sap, mekong river basin. *Envi-
598 ronmental Fluid Mechanics* , 1–29.

- 599 Le Hénaff, M., Kourafalou, V.H., Paris, C.B., Helgers, J., Aman, Z.M., Hogan,
600 P.J., Srinivasan, A., 2012. Surface evolution of the Deepwater Horizon
601 oil spill patch: Combined effects of circulation and wind-induced drift.
602 Environmental Science & Technology 46, 7267–7273.
- 603 Lee, T.N., Leaman, K., Williams, E., Berger, T., Atkinson, L., 1995. Florida
604 Current meanders and gyre formation in the southern Straits of Florida.
605 Journal of Geophysical Research: Oceans 100, 8607–8620.
- 606 Lee, T.N., Mayer, D.A., 1977. Low-frequency current variability and spin-off
607 eddies along the shelf off southeast Florida. Collected Reprints 1, 344.
- 608 Lee, T.N., Smith, N., 2002. Volume transport variability through the Florida
609 Keys tidal channels. Continental Shelf Research 22, 1361–1377.
- 610 Lee, T.N., Williams, E., 1988. Wind-forced transport fluctuations of the
611 Florida Current. Journal of Physical Oceanography 18, 937–946.
- 612 Li, Z., Johns, B., 1998. A three-dimensional numerical model of surface
613 waves in the surf zone and longshore current generation over a plane beach.
614 Estuarine, Coastal and Shelf Science 47, 395–413.
- 615 Lin, N., Chavas, D., 2012. On hurricane parametric wind and applications in
616 storm surge modeling. Journal of Geophysical Research: Atmospheres 117.
- 617 Liu, Y., Weisberg, R.H., 2012. Seasonal variability on the West Florida shelf.
618 Progress in Oceanography 104, 80–98.
- 619 Liu, Y., Weisberg, R.H., Zheng, L., 2020. Impacts of hurricane Irma on the
620 circulation and transport in Florida Bay and the Charlotte Harbor estuary.
621 Estuaries and Coasts 43, 1194–1216.
- 622 Liubartseva, S., Coppini, G., Lecci, R., Clementi, E., 2018. Tracking plastics
623 in the Mediterranean: 2D Lagrangian model. Marine Pollution Bulletin
624 129, 151–162.

- 625 Longuet-Higgins, M.S., 1970. Longshore currents generated by obliquely
626 incident sea waves. *Journal of geophysical research* 75, 6778–6789.
- 627 Longuet-Higgins, M.S., Stewart, R., 1964. Radiation stresses in water waves;
628 a physical discussion, with applications, in: Deep sea research and oceano-
629 graphic abstracts, Elsevier. pp. 529–562.
- 630 Madsen, O.S., Poon, Y.K., Gruber, H.C., 1989. Spectral wave attenuation by
631 bottom friction: Theory, in: *Coastal Engineering 1988*, pp. 492–504.
- 632 Malmstadt, J., Scheitlin, K., Elsner, J., 2009. Florida hurricanes and damage
633 costs. *Southeastern Geographer* 49, 108–131.
- 634 McWilliams, J.C., Restrepo, J.M., Lane, E.M., 2004. An asymptotic theory
635 for the interaction of waves and currents in coastal waters. *Journal of Fluid
636 Mechanics* 511, 135.
- 637 McWilliams, J.C., Sullivan, P.P., 2000. Vertical mixing by Langmuir circula-
638 tions. *Spill Science & Technology Bulletin* 6, 225–237.
- 639 Mei, C.C., 1989. The applied dynamics of ocean surface waves. volume 1.
640 World scientific.
- 641 Moon, I.J., Ginis, I., Hara, T., Thomas, B., 2007. A physics-based parame-
642 terization of air-sea momentum flux at high wind speeds and its impact on
643 hurricane intensity predictions. *Monthly Weather Review* 135, 2869–2878.
- 644 Pinelli, J.P., Roueche, D., Kijewski-Correa, T., Plaz, F., Prevatt, D., Zisis,
645 Elawady, A., Haan, F., Pei, S., Gurley, K., et al., 2018. Overview of
646 damage observed in regional construction during the passage of Hurricane
647 Irma over the State of Florida, in: *Forensic Engineering 2018: Forging
648 Forensic Frontiers*. American Society of Civil Engineers Reston, VA, pp.
649 1028–1038.

- 650 Powell, M.D., Houston, S.H., Amat, L.R., Morisseau-Leroy, N., 1998. The
651 HRD real-time hurricane wind analysis system. *Journal of Wind Engineering*
652 and Industrial Aerodynamics 77, 53–64.
- 653 Powell, M.D., Vickery, P.J., Reinhold, T.A., 2003. Reduced drag coefficient
654 for high wind speeds in tropical cyclones. *Nature* 422, 279–283.
- 655 Röhrs, J., Christensen, K.H., Hole, L.R., Broström, G., Drivdal, M., Sundby,
656 S., 2012. Observation-based evaluation of surface wave effects on currents
657 and trajectory forecasts. *Ocean Dynamics* 62, 1519–1533.
- 658 Schott, F.A., Lee, T.N., Zantopp, R., 1988. Variability of structure and
659 transport of the Florida Current in the period range of days to seasonal.
660 *Journal of Physical Oceanography* 18, 1209–1230.
- 661 Siadatmousavi, S.M., Jose, F., Stone, G., 2011. Evaluation of two WAM
662 white capping parameterizations using parallel unstructured SWAN with
663 application to the Northern Gulf of Mexico, USA. *Applied Ocean Research*
664 33, 23–30.
- 665 Sikirić, M.D., Roland, A., Janeković, I., Tomazić, I., Kuzmić, M., 2013.
666 Coupling of the Regional Ocean Modeling System (ROMS) and Wind
667 Wave Model. *Ocean Modelling* 72, 59–73.
- 668 Smith, N.P., 1982. Response of Florida Atlantic shelf waters to hurricane
669 David. *Journal of Geophysical Research: Oceans* 87, 2007–2016.
- 670 Stokes, G.G., 1880. On the theory of oscillatory waves. *Transactions of the*
671 *Cambridge Philosophical Society* .
- 672 Tolman, H.L., et al., 2009. User manual and system documentation of
673 WAVEWATCH III TM version 3.14. Technical note, MMAB Contribution
674 276, 220.

- 675 Van Den Bremer, T., Breivik, Ø., 2018. Stokes drift. Philosophical Transactions of the Royal Society A: Mathematical, Physical and Engineering Sciences 376, 20170104.
- 678 Villas Bôas, A.B., Cornuelle, B.D., Mazloff, M.R., Gille, S.T., Arduin, F.,
679 2020. Wave-current interactions at meso-and submesoscales: Insights from
680 idealized numerical simulations. Journal of Physical Oceanography 50,
681 3483–3500.
- 682 Wachnicka, A., Browder, J., Jackson, T., Louda, W., Kelble, C., Abdelrahman,
683 O., Stabenau, E., Avila, C., 2019. Hurricane Irmas impact on water quality
684 and phytoplankton communities in Biscayne Bay (Florida, USA). Estuaries and Coasts , 1–18.
- 686 Weisberg, R., Liu, Y., Mayer, D., 2009. Mean circulation on the west Florida
687 continental shelf observed with long-term moorings. Geophys. Res. Lett
688 36, L19610.
- 689 Weisberg, R.H., Zheng, L., 2006. Hurricane storm surge simulations for
690 Tampa Bay. Estuaries and Coasts 29, 899–913.
- 691 Wu, L., Chen, C., Guo, P., Shi, M., Qi, J., Ge, J., 2011. A FVCOM-
692 based unstructured grid wave, current, sediment transport model, I. Model
693 description and validation. Journal of Ocean University of China 10, 1–8.
- 694 Xian, S., Feng, K., Lin, N., Marsooli, R., Chavas, D., Chen, J., Hatzikyriakou,
695 A., 2018. Brief communication: Rapid assessment of damaged residential
696 buildings in the Florida Keys after Hurricane Irma. Natural Hazards and
697 Earth System Sciences 18, 2041–2045.
- 698 Zedler, S., Niiler, P., Stammer, D., Terrill, E., Morzel, J., 2009. Ocean's
699 response to Hurricane Frances and its implications for drag coefficient
700 parameterization at high wind speeds. Journal of Geophysical Research: Oceans 114.

702 Zhang, C., Durgan, S.D., Lagomasino, D., 2019. Modeling risk of mangroves
703 to tropical cyclones: A case study of Hurricane Irma. *Estuarine, Coastal*
704 and *Shelf Science* 224, 108–116.